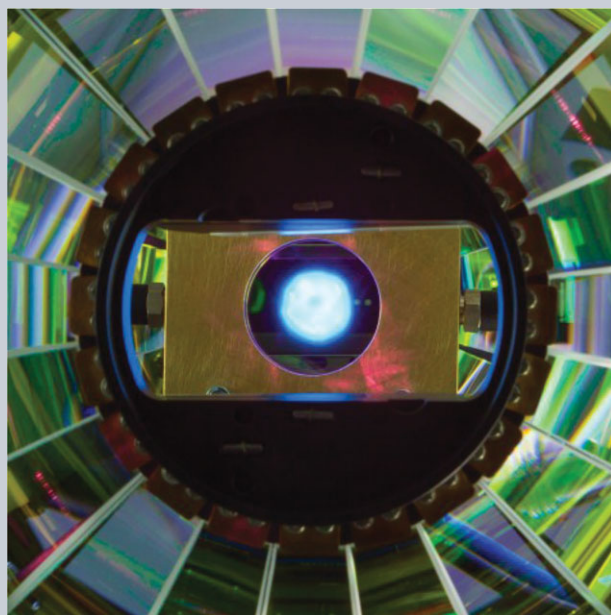


**Abstract** An analytical model is presented describing the temporal intensity contrast determined by amplified spontaneous emission in high-intensity laser systems which are based on the principle of chirped pulse amplification. The model describes both the generation and the amplification of the amplified spontaneous emission for each type of laser amplifier. This model is applied to different solid state laser materials which can support the amplification of pulse durations  $\leq 350$  fs. The results are compared to intensity and fluence thresholds, e.g. determined by damage thresholds of a certain target material to be used in high-intensity applications. This allows determining if additional means for contrast improvement, e.g. plasma mirrors, are required for a certain type of laser system and application. Using this model, the requirements for an optimized high-contrast front-end design are derived regarding the necessary contrast improvement and the amplified “clean” output energy for a desired focussed peak intensity. Finally, the model is compared to measurements at three different high-intensity laser systems based on Ti:Sapphire and Yb:glass. These measurements show an excellent agreement with the model.



## The generation of amplified spontaneous emission in high-power CPA laser systems

Sebastian Keppler<sup>1,\*</sup>, Alexander Sävert<sup>1</sup>, Jörg Körner<sup>1</sup>, Marco Hornung<sup>1,2</sup>, Hartmut Liebetrau<sup>1</sup>, Joachim Hein<sup>1,2</sup>, and Malte Christoph Kaluza<sup>1,2</sup>

### 1. Introduction

Over the last decade, we have witnessed a tremendous progress in the field of relativistic laser-plasma interactions, in particular in laser-driven particle acceleration. Enabled by the rapid development of high-power laser systems, potential applications based on table-top relativistic laser-electron accelerators [1] or on laser-driven ion sources [2] have come closer to reality. With the availability of such compact pulsed particle sources, the generation of ultra-short secondary XUV and x-ray pulses [3] or medical applications based on intense ion beams [4] could be realized in university-scale laboratories. This would bring a large variety of potential applications closer to reality, which are currently limited to large-scale accelerator facilities. Such plasma-particle accelerators rely on the availability of high-power laser pulses which can be focussed to intensities in excess of  $I_0 = 10^{21}$  W/cm<sup>2</sup> [5, 6]. The ongoing development of such laser systems, in particular towards higher laser pulse energies and shorter

pulse durations, have led to higher kinetic energies of accelerated electrons [1], protons and heavier ions [2].


To reach such high intensities in the laboratory, various classes of laser systems based on chirped pulse amplification (CPA) [7] are currently used. They can be classified according to the active laser material. On the one hand hybrid optical parametric chirped-pulse amplification (OPCPA) Nd:glass laser systems typically provide one pulse per hour with an amplified pulse energy of up to  $E_{\text{pulse}} = 186$  J within a pulse duration down to  $\tau_{\text{pulse}} \leq 167$  fs [8]. On the other hand Ti:Sapphire laser systems deliver pulses with an energy up to  $E_{\text{pulse}} = 50$  J with pulse durations of  $\tau_{\text{pulse}} \leq 30$  fs [6, 9] at a repetition rate of 0.1 . . . 10 Hz. Furthermore, diode-pumped laser systems, based on Yb<sup>3+</sup>-doped glass [10] or CaF<sub>2</sub> [11], are a promising alternative currently providing up to  $E_{\text{pulse}} = 14.3$  J on target within a pulse duration of  $\tau_{\text{pulse}} \leq 145$  fs at a repetition rate of 0.025 Hz [12, 13].

Key parameters of the different types of laser systems which are immediately relevant for applications (e.g. the

<sup>1</sup> Institute of Optics and Quantum Electronics, Friedrich-Schiller-University of Jena, Germany

<sup>2</sup> Helmholtz-Institute Jena, Germany

\*Corresponding author: e-mail: Sebastian.Keppler@uni-jena.de

 This is an open access article under the terms of the Creative Commons Attribution-NonCommercial License, which permits use, distribution and reproduction in any medium, provided the original work is properly cited and is not used for commercial purposes.

wavelength, pulse duration and pulse energy) are well understood and can be compared respectively. However, it has been found that the temporal intensity contrast (TIC) is another crucial parameter for high-intensity laser-matter interactions. Intense prepulses and amplified spontaneous emission (ASE) which irradiate the target prior to the arrival of the main pulse can produce a preplasma on the target's front surface altering the target significantly [14] and even rendering the desired particle acceleration impossible. So far, the temporal intensity contrast has been characterized for each laser system individually and – for most cases – at reduced peak energy. Experimentally validated theoretical simulations of the contrast influenced by the complete laser system, which would allow for the comparison of the different classes of high-power laser systems in terms of the contrast, do not exist up until now.

The contributions affecting the temporal intensity contrast can be roughly divided into four categories: (i) prepulses on the scale of the main pulse duration generated on nanosecond (ns)-time scales before the main pulse due the architecture of the laser system, which are mainly caused by pulses leaking through the pulse picker behind a MHz oscillator or out of regenerative amplifiers [21]; (ii) prepulses on the scale of the main pulse duration on picosecond (ps)-time scales mainly generated by nonlinear mixing of postpulses, generated in thin transmissive optics, which temporally overlap with the stretched main pulse during amplification [22, 23]; (iii) deterioration of the rising slope of the main pulse, mainly due to uncompensated higher-order spectral phase modulations [24], which can also be caused by scattered light from the stretcher's grating [25], or by spectral clipping [26], and finally (iv) ASE, caused by fluorescence emitted in the different amplification stages of the laser [27]. Since the contribution from (i), (ii) and (iii) strongly depend on the architecture of the individual laser system and can in principle be reduced by an appropriate choice of the optical elements, we will concentrate in this paper on the generation of ASE, which primarily depends on the active material used in the amplifiers and cannot be suppressed completely.

The temporal intensity contrast is defined as the ratio between the main pulse peak intensity  $I_0$  and the intensity  $I(t)$  at times before ( $t < 0$ ) or after ( $t > 0$ ) the arrival of the main pulse, i. e.  $\text{TIC}(t) = I_0/I(t) \geq 1$ . However, for the characterization of complete laser systems we believe that it may be more intuitive to use the prepulse intensity normalized to the main pulse intensity,  $I(t)/I_0 \leq 1$ , which is equal to  $\text{TIC}^{-1}$ . For a given laser peak intensity and a certain ablation threshold of the target material, using this parameter allows to quickly estimate if additional means of contrast enhancement techniques, e. g. plasma mirrors, are necessary for certain applications. Due to this reason we will use the inverted temporal intensity contrast  $\text{TIC}^{-1}$  in the following mathematical derivations and measurements. Note that when using this terminology a “high contrast” corresponds to low values of the inverted contrast.

For a successful and reproducible application of particle radiation generated during relativistic laser-plasma interactions, the physics underlying the acceleration

processes needs to be fully understood. Nevertheless, empirical evidence points toward the driving laser pulse as a major contributor in producing stable and reliable experimental results. Besides the obvious parameters like pulse energy, duration, and farfield profile, the temporal intensity contrast is a key component of the driving laser pulse. In order to optimize this contrast in high-power laser systems, the physical limitations of the minimum achievable contrast have to be derived and the dependencies on relevant parameters, such as the laser material, the small signal gain, amplifier losses etc., have to be investigated. Using these results, the optimal design for a contrast optimized laser front-end design can be derived. This is particularly important if intensity-dependent contrast improvement methods are required. Such methods typically involve using a double CPA (DCPA) system [15] combined with either cross polarized wave generation (XPW) [16] or saturable absorbers [17], using an OPCPA setup [18], or using a plasma mirror [19]. Due to the non-linear nature and the limited efficiency of these processes, the performance of the laser system is significantly affected. Thus, the application of these methods should be reduced to a minimum necessary for the reliable realization of a specific laser plasma interaction.

Furthermore, a comprehensive understanding of the ASE generation is also of interest for systems, which are already operational and which have already been improved with respect to their contrast. As a result of the application of different contrast enhancement methods, the TIC is often below the detection-limit of state-of-the-art 3<sup>rd</sup>-order cross-correlators, which is typically  $\text{TIC}_{\text{min}}^{-1} = 10^{-10} \dots 10^{-12}$  [20]. However, even at this level, the pulse contrast can still significantly influence experiments, since focusing the main pulse to intensities in excess of  $10^{21} \text{ W/cm}^2$  leads to on-target prepulse intensities on the order of  $10^9 \text{ W/cm}^2$ , which – depending on the duration of this irradiation – can already affect the target conditions. Furthermore, state-of-the-art TIC measurement techniques usually measure the relative contrast in the near-field of the laser pulse. However, in high-intensity laser-matter interactions one is interested in the pulse contrast in the far-field (i. e. in the focussed beam), therefore – strictly speaking – this method only provides information on the evolution of the power contrast. The power contrast can only be converted into an intensity contrast when the prepulses and ASE have the same focusability as the main pulse, which is not necessarily the case in particular for power amplifiers with a non-imaging architecture. However, as it will be shown, in that case the near-field measurement provides a “worst-case-scenario”, since the focusability of the ASE in general cannot be better than the main pulse itself. Hence, the TIC often has to be estimated, which requires a detailed study of the various laser systems capable of generating these high-power pulses.

Finally, the calculation of the TIC plays a crucial role for the design and scaling of new and existing high-power laser systems. Once the peak intensity of a laser system is increased by a certain factor, the TIC needs to be improved by at least the same factor if a certain on-target intensity threshold of the prepulse may not be exceeded. However,

improving the contrast of the amplifier, which is generating the main part of the ASE by this certain factor, does not necessarily improve the TIC of the whole laser system by the same factor, since all subsequent amplifiers may also influence the final ASE level. Hence, the limiting amplifier has to be identified before any contrast enhancement systems are designed and scaled for the specific application. Thus, the ultimate success of all contrast improvement methods strongly relies on a systematic study of the ASE generation in high-power laser systems.

Different approaches have been followed so far to describe the ASE of high-power laser systems. Koechner et al. [28] proposed a model which can be applied to multipass amplifiers utilizing laser rods, in which the acceptance solid angle of the ASE is determined by the geometry of the laser rod itself. However, in many laser systems, amplifier disks rather than rods are used, with a thickness much shorter than the Rayleigh-length of the laser beam. In such amplifiers the beam waist is positioned in the centre of the amplifying medium in order to get an ideal overlap of the pump beam with the laser beam. Hence, the acceptance solid angle for the ASE is determined by the amplifier mode only and does not depend on the specific amplifier geometry. Furthermore, it is not enlarged by refraction at the surfaces, since the laser beam may be assumed to be perfectly collimated while passing through the amplifier disks. Regarding high-power OPCPA systems, Ross et al. [29] made a general consideration of the on-target ASE intensity. However, this estimation has not been validated experimentally.

Here, we present a model for the calculation of the physical ASE limits of conventional laser gain media assuming  $d \leq z_R$  with  $d$  being the thickness of the media and  $z_R$  being the Rayleigh-length of the laser beam. Our model is a further development of the approach followed by Ivanov et al. [27] taking into account losses, which allows for the description of 3-level materials, such as  $\text{Yb}^{3+}$ -doped glasses or crystals as they are often used in diode-pumped laser systems. In Section 2, the generation of the ASE is described and the applicability of the model to different types of amplifiers is discussed. The parameters with the strongest influence, e.g. the small signal gain and losses in the amplifiers, are discussed in detail and the minimum achievable  $\text{TIC}^{-1}$  is compared for different state-of-the-art amplification media. In Section 3, the time-dependent ASE amplification is described where saturation is also taken into account. Furthermore, the scaling of a necessary contrast enhancement and “clean” output energy with respect to a certain focussed intensity is presented in Section 4 for given threshold values. Here, the “clean” output energy describes the energy of the ASE adjusted main pulse behind the contrast enhancement system. In Section 5, we finally compare our model with detailed measurements carried out at the JETI200 (Ti:Sapphire, 200 TW peak power), the JETI40 (Ti:Sapphire, 40 TW) and the POLARIS [13, 30] (Yb:FP20 fluorophosphate glass [10], 100 TW) laser systems, which are operated at the Helmholtz-Institute Jena and the Friedrich-Schiller-University of Jena. The model shows a very good agreement with the measured  $\text{TIC}^{-1}$  for these three different laser systems.

## 2. The generation of ASE

Fluorescence is emitted by an active material in which a population inversion has been generated due to an external stimulation. The small signal gain  $g_0$  is connected to the population inversion through:

$$g_0 = \exp \left[ d \cdot (N_0 \sigma_{\text{em}} - (N_{\text{dop}} - N_0) \sigma_{\text{abs}}) \right] \quad (1)$$

with  $N_0$  being the initial excitation density of the laser active ions in the laser material;  $d$  being its thickness and  $\sigma_{\text{em}}$  and  $\sigma_{\text{abs}}$ , the emission and absorption cross sections for the laser wavelength of a monochromatic laser beam, respectively.  $N_{\text{dop}}$  represents the doping concentration of the laser material. For a comprehensive description including a reduction of the gain due to losses, which may be caused by cavity losses, impurities or reabsorption at the laser wavelength as it occurs in Yb-doped 3-level laser materials, a loss term  $L$  is introduced. Reabsorption can be described by  $L = 1 - \exp[-N_{\text{dop}} \sigma_{\text{abs}} d]$ , which finally leads to:

$$g_0 = (1 - L) \exp \left[ N_0 d (\sigma_{\text{em}} + \sigma_{\text{abs}}) \right], \quad (2)$$

The excited active ions in the laser material decay exponentially with the radiative lifetime  $\tau_{\text{rad}}$  which leads to spontaneous emission of fluorescence light. Note that the fluorescence lifetime  $\tau_f$  differs from the radiative lifetime once additional transitions to other lower-lying energy levels or quenching processes are possible, involving for example the de-excitation at impurities or crystal defects, or energy transfers between different laser ions. However, these losses result in a smaller efficiency of the pumping process and are not considered in this model.

Using the saturation intensity, which is defined as  $I_{\text{sat}} = (h \cdot \nu) / [(\sigma_{\text{em}} + \sigma_{\text{abs}}) \tau_{\text{rad}}]$ , the total power of the fluorescence light  $P_F$  at times  $t \ll \tau_{\text{rad}}$  can be written as

$$\begin{aligned} P_F &= \frac{h\nu}{(\sigma_{\text{em}} + \sigma_{\text{abs}}) \tau_{\text{rad}}} \cdot A \cdot \ln \left[ \frac{g_0}{1 - L} \right] \\ &= I_{\text{sat}} \cdot A \cdot \ln \left[ \frac{g_0}{1 - L} \right]. \end{aligned} \quad (3)$$

with  $h\nu$  being the energy of a photon and  $A$  being the pumped area.

The fluorescence power is emitted – in accordance with the spectral characteristic of the laser material – within a solid angle of  $4\pi$  from the pumped area  $A$ . However, common laser amplifiers have a limited spectral, spatial, and – in case of regenerative amplifiers (RAs) –, even a limited temporal acceptance. Considering the amplification of a laser pulse with a spectral bandwidth  $\Delta\nu$  and a small signal gain  $\bar{g}$ , which is averaged over  $\Delta\nu$ , the fluorescence power, which is accepted in the first pass of the amplifier,  $P_F^{(1)}$  can be estimated to

$$P_F^{(1)} = \bar{I}_{\text{sat}} K_{\Delta\Omega} K_{\Delta\nu} K_p \ln \left[ \frac{\bar{g}_0}{1 - \bar{L}} \right]. \quad (4)$$

Here, the parameter  $K_{\Delta\Omega} = \Delta\Omega A/4\pi$  describes the spatio-angular and  $K_{\Delta\nu}$  the spectral acceptance of the amplifier. Due to the wavelength dependency,  $I_{\text{sat}}$  also has to be considered as the averaged value over the spectral bandwidth. The parameter  $K_p$  describes the probability of an emitted photon to match the polarization direction of the amplifier under consideration. This is of particular importance when anisotropic laser crystals, such as Ti:Sapphire, are considered.

If the evolution of the amplification process is considered as a geometric series, as shown by Ivanov et al. [27], the ASE power, defined as the amplified spontaneous emitted fluorescence power, after  $n$  passes is given by

$$P_{\text{ASE}}^{(n)} \approx P_{\text{F}}^{(1)} \frac{\bar{G}}{\bar{g}_0 - 1}, \quad (5)$$

with  $\bar{G} = \bar{g}_0^n$  being the averaged overall small signal gain of the amplifier.

Assuming a comparable focusing of the ASE and the main pulse, which has been measured experimentally for RAs [33], the minimal achievable  $\text{TIC}^{-1}$  of such kind of amplifiers can be expressed by

$$\begin{aligned} \text{TIC}_{\text{ASE}}^{-1} &= \frac{I_{\text{ASE}}}{I_{\text{pulse}}} = \frac{P_{\text{ASE}}}{P_{\text{pulse}}} \\ &= \bar{I}_{\text{sat}} K_{\Delta\Omega} K_p K_{\Delta\nu} \gamma(\bar{g}_0, \bar{L}) \frac{\tau_{\text{pulse}}}{E_{\text{seed}}}, \end{aligned} \quad (6)$$

with

$$\gamma(\bar{g}_0, \bar{L}) = \frac{\ln[\bar{g}_0/(1 - \bar{L})]}{\bar{g}_0 - 1}. \quad (7)$$

The main pulse power  $P_{\text{pulse}}$  can be calculated by  $P_{\text{pulse}} = E_{\text{seed}} \cdot \bar{G}/\tau_{\text{pulse}}$ . Here,  $E_{\text{seed}}$  is the seed energy and  $\tau_{\text{pulse}}$  is the final compressed pulse duration.  $\gamma(\bar{g}_0, \bar{L})$  describes the dependency of the  $\text{TIC}^{-1}$  on the small signal gain and on losses as discussed in the following section.

### Small signal gain and losses

The small signal gain and losses are fundamental parameters of the ASE generated by a certain amplifier. Their influence on the  $\text{TIC}^{-1}$  is described by  $\gamma(\bar{g}_0, \bar{L})$ . Here,  $\gamma(\bar{g}_0, 0\%) = 1$  corresponds to a very low gain ( $\bar{g} \approx 1$ ) and negligible losses. Note that  $\bar{g}_0 = 1$  in Eq. 7 cannot be interpreted physically, since the estimated limit of the geometrical series for the amplification dynamics of the ASE is only valid for  $\bar{g}_0 > 1$ . Furthermore, the validity of the limit of the geometrical series has been assumed for all  $\bar{g} > 1$ , which requires a sufficiently large number of amplification passes.

Fig. 1 shows  $\gamma(\bar{g}_0, \bar{L})$  for different relative amplifier losses. It has been found that for low gain values, even low losses can lead to drastic deterioration of the  $\text{TIC}^{-1}$  of more than one order of magnitude. If losses occur, a

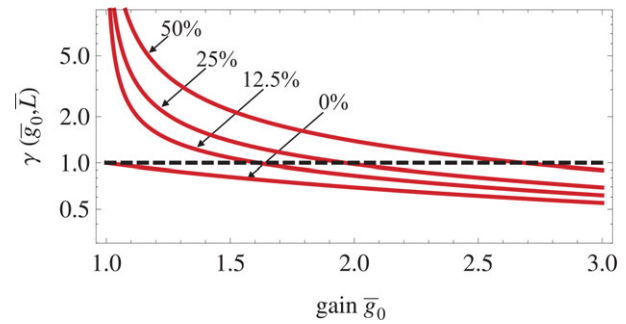


**Figure 1** Logarithmic plot of the  $\text{TIC}^{-1}$  deterioration, represented by  $\gamma(\bar{g}_0, \bar{L})$ , depending on the small signal gain for losses of 0%, 12.5%, 25% and 50%. The horizontal dashed line represents the criterion for the derivation of Eq. (8).

higher excitation density is necessary in order to maintain the gain value. This in turn leads to an increased ASE power. Furthermore, at low gain levels, the relative contribution of the accepted fluorescence power per pass preserves its relevance for a large number of amplification passes. If a higher gain is considered, the relative contribution of the accepted fluorescence power per pass can be neglected after a few passes already.

Losses, however, can often not be avoided within the amplifiers of a high-power laser front-end. In order to avoid a significant deterioration of the  $\text{TIC}^{-1}$ , a loss-dependent minimum small signal gain  $\bar{g}_{0,\text{min}}$  has to be realized. This is described by Eq. (8), which allows one to calculate the minimum gain which would be necessary for  $\gamma(\bar{g}_0, \bar{L}) \leq 1$  which is equivalent to a low-gain amplifier with negligible losses:

$$\bar{g}_{0,\text{min}}(\bar{L}) \geq -W_{-1} \left[ \frac{1 - \bar{L}}{e} \right] \approx 2.8 \bar{L} + 1.3. \quad (8)$$

Here,  $W_{-1}$  corresponds to the Lambert-W-function for the lower branch ( $W \leq -1$ ) [31]. If the condition, derived for the minimum small signal gain, is satisfied, the calculation of the overall  $\text{TIC}^{-1}$  simplifies to:

$$\text{TIC}_{\text{ASE}}^{-1} = \bar{I}_{\text{sat}} K_{\Delta\Omega} K_p K_{\Delta\nu} \frac{\tau_{\text{pulse}}}{E_{\text{seed}}}, \quad (9)$$

which only depends on the properties of the laser material and on the main pulse parameters  $E_{\text{seed}}$  and  $\tau_{\text{pulse}}$ .

### Spectral- ( $K_{\Delta\nu}$ ) and polarization acceptance ( $K_p$ )

The spectral acceptance  $K_{\Delta\nu}$  of an amplifier is defined as the spectral fraction of the totally emitted fluorescence which can actually be amplified within the considered amplifier. Here, the reflectivity of the used laser mirrors has to be considered. A certain spectral part of the fluorescence is accepted, when the mirrors provide a reflectivity of  $R \geq 99.9\%$ . Furthermore, in many cases the amplifiers only emit a bandwidth which is a small fraction of the total bandwidth supported by the laser material. Hence, limiting

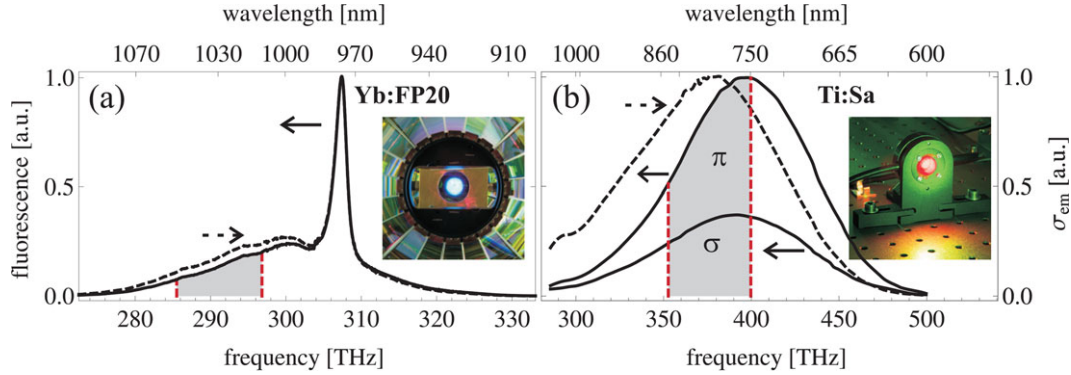


**Figure 2** Relative fluorescence spectrum of Yb:FP20 (left, solid line) and relative fluorescence spectrum of Ti:Sapphire for  $\pi$ - and  $\sigma$ -polarizations (right, solid lines) [52]. The vertical red dashed lines represent the boundaries of the spectral acceptance of the POLARIS-RA and the JETI200-RA, respectively, according to the mirror specifications of  $R \geq 99.9\%$ . The relative emission cross sections for the laser polarization are represented by the black dashed lines in both figures. The insets show photographs of the pumped Yb:FP20 (in POLARIS) and Ti:Sapphire (in JETI), where the fluorescence is clearly visible. Note that the emission of Yb:FP20 in the visible range is dominated by up-converted fluorescence light due to contaminations of other rare-earth ions.

the spectral acceptance of the amplifier immediately leads to an improvement of the  $\text{TIC}^{-1}$ .

As examples, the spectral characteristics for Ti:Sapphire and Yb:FP20 are plotted in Fig. 2. Here, the materials and the acceptance parameters corresponds to both JETI-systems (Ti:Sapphire) and to POLARIS (Yb:FP20). These systems are discussed in detail in section 5. The gray shaded areas in Fig. 2 represent the spectral windows emitted by the respective laser systems. Here it is apparent that the fluorescence spectrum  $F(\nu)$  is typically not symmetric around the central frequency of the laser pulse. Hence, the accepted fluorescence of the amplifier,  $\int_{\Delta\nu} F(\nu') d\nu'$ , must be considered for the calculation of  $K_{\Delta\nu}$  in relation to the fluorescence,  $\int_{\nu} F(\nu') d\nu'$ , emitted over the full spectrum.

Since amplifiers are mainly polarization sensitive, only fluorescence with the correct polarization state for the amplifier is accepted. The probability of an emitted photon to match this polarization state is described by the polarization acceptance parameter  $K_p$ . Considering isotropic media, such as Yb:FP20, the probability is equal for both polarization directions, hence  $K_p = 0.5$ . However, considering anisotropic materials, such as Ti:Sapphire, the probability of a photon emission differs for both polarization directions, which also results in different fluorescence spectra and thus a polarization sensitive small signal gain. The fluorescence spectra of both polarization states for Ti:Sapphire are shown in Fig. 2. For an amplifier accepting the  $\pi$ -polarization,  $K_{p\pi}$  is calculated considering the ratio of the fluorescence spectra, integrated over the spectral acceptance

$$K_{p\pi} = \frac{\int_{\Delta\nu} F_{\pi}(\nu') d\nu'}{\int_{\Delta\nu} F_{\sigma}(\nu') d\nu' + \int_{\Delta\nu} F_{\pi}(\nu') d\nu'}. \quad (10)$$

It has been found, that for all materials which are considered in this paper,  $K_p$  can be assumed to be constant for all spectral bandwidths. Table 2 shows the values for  $K_p$  for all considered materials.

### Spatio-angular acceptance ( $K_{\Delta\Omega}$ )

For the derivation of Eq. (6) and Eq. (9), the spatio-angular acceptance was introduced as the product of the acceptance solid angle and the size of the pumped area  $K_{\Delta\Omega} = \Delta\Omega/4\pi \cdot A$ . If in an amplifier the minimum achievable  $\text{TIC}^{-1}$  is regarded, only the amplification of the  $\text{TEM}_{00}$ -mode has to be considered. Here, the solid angle can be determined using the divergence of the  $\text{TEM}_{00}$ -mode which is defined by the beam-parameter product [34]. As a consequence, the spatio-angular acceptance of the amplifier can be simplified to [32]

$$K_{\Delta\Omega}^{\text{RA}} = \frac{\Delta\Omega}{4\pi} \cdot A = \frac{\lambda^2}{4\pi}. \quad (11)$$

The simplification is valid if amplifiers are considered, which accept the  $\text{TEM}_{00}$ -mode only. This corresponds to the mode which is amplified in a common RA, but which can also be achieved by strong spatial or modal filtering. Since in high-power laser systems an oscillator typically generates laser pulses with  $\sim \text{nJ}$  energy, RAs are often used for the amplification into the mJ-regime. As a consequence, the fluorescence accepted by the amplifier is independent of the size of the pumped area. Hence, amplifiers having a large pumped area in order to amplify the pulse to higher output energies, provide the same  $\text{TIC}^{-1}$  as amplifiers with a small pumped area and a lower designed output energy. In contrast to RAs, multipass amplifiers typically do not form a resonator. The spatio-angular acceptance here is mainly defined by the imaging optics (e.g. magnification telescopes) and the aperture of the used laser mirrors. This fact eventually leads to a larger focal spot of the ASE contribution generated in these amplifiers.

In Ref. [33], a detailed measurement of the  $\text{TIC}^{-1}$  regarding the different amplification stages of the POLARIS laser system is described. The investigation comprises the measured  $\text{TIC}^{-1}$  as well as an absolute on-target ASE

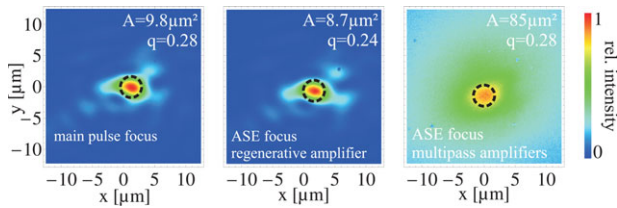


**Figure 3** Focal spot measurement (left) of the main pulse, (middle) of the ASE generated by the first RA and (right) of the multipass amplifiers carried out at the POLARIS laser system with an  $f/3$  focussing. The dashed circle in all three plots represents the FWHM-area of the main pulse. The measurement as well as the amplifier setup are described in [33].

characterization of the first (A1) and second RA (A2) as well as all multipass amplifiers. The  $\text{TIC}^{-1}$  was measured using different detectors including a 3<sup>rd</sup>-order cross-correlator and photo-diodes with calibrated ND filters which allowed for the measurement in the nearfield. Furthermore, the energy, the duration and the focusability of the different ASE contributions of the considered amplifier were measured, which allow for the determination of the absolute ASE intensity in the farfield. Fig. 3 shows the focal spot of the main pulse (left), of the ASE from the first RA (middle) and the ASE from all multipass amplifiers (right) of POLARIS. The ASE focusability of both types of amplifiers, the RAs and the multipass amplifiers, differs significantly.

When considering high-intensity laser-plasma interactions, the fraction of the ASE enclosed within the FWHM area of the main pulse focus is of relevance only. This is represented by the black dashed circular overlay in Fig. 3. Since the FWHM-intensity for laser-plasma experiments is calculated by  $I = q \cdot E / (\tau \cdot A)_{\text{pulse}}$ , with  $q$  being the fraction of energy included within the FWHM-area,  $A_{\text{pulse}}$ , of the main pulse, the ASE intensity of the multipass amplifiers has to be calculated in the same way. However, since only this ASE fraction is of relevance, it follows that assuming the divergence angle of the main pulse as the spatio-angular acceptance of the relevant ASE fraction generated by the multipass amplifiers is sufficient for the estimation of the  $\text{TIC}^{-1}$  regarding multipass amplifiers. However, in this case, the potential enlargement of the main pulse divergence due to aberrations has to be taken into account. Distorted optical surfaces as well as thermal aberrations of the pumped amplifying media can lead to aberrations which deteriorate the focusability of the main pulse. The resulting enlargement of the divergence of the main pulse can be described by the  $M^2$  factor of both spatial directions  $M_x^2 \times M_y^2$ . Hence, the resulting spatio-angular acceptance of a multipass amplifier  $K_{\Delta\Omega}^{\text{MA}}$  can be calculated by:

$$K_{\Delta\Omega}^{\text{MA}} = \frac{\lambda^2}{4\pi} \cdot (M_x^2 \times M_y^2) \quad (12)$$

In Table 1, the results from [33] of the  $\text{TIC}^{-1}$  measurement performed in the nearfield ( $\text{TIC}_{\text{NF}}^{-1}$ ) are compared

**Table 1** Comparison of different  $\text{TIC}^{-1}$  measurement methods and the  $\text{TIC}^{-1}$  calculation for both regenerative and multipass amplifiers operating in the POLARIS laser system. The different methods are a relative  $\text{TIC}^{-1}$  measurement in the nearfield of the laser beam ( $\text{TIC}_{\text{NF}}^{-1}$ ), a measurement based on the averaged intensity via energy, duration and focal spot determination ( $\text{TIC}_I^{-1}$ ) and the calculation of the  $\text{TIC}^{-1}$  using Eq. (6) ( $\text{TIC}_{\text{calc}}^{-1}$ ). A detailed description of the  $\text{TIC}^{-1}$  measurements and the POLARIS architecture are given in [33].

Measured $\text{TIC}_{\text{NF}}^{-1}$	Measured $\text{TIC}_I^{-1}$	$\text{TIC}_{\text{calc}}^{-1}$
First RA: (A1)		
$3.6 \times 10^{-9}$	$8.0 \times 10^{-10}$	$8.4 \times 10^{-10}$
Second RA: (A2)		
$4.8 \times 10^{-13}$	$1.7 \times 10^{-13}$	$1.7 \times 10^{-13}$
Multipass amplifiers (A2.5 - A4)		
$4.6 \times 10^{-16}$	$2.4 \times 10^{-17}$	$3.9 \times 10^{-17}$

to the  $\text{TIC}^{-1}$ , determined in the farfield by measuring the absolute ASE intensity of the different amplifiers ( $\text{TIC}_I^{-1}$ ). Here we found a significant difference of both measurement methods which is due to the different focal spot sizes of the ASE and the main pulse [33]. The calculated  $\text{TIC}^{-1}$  using Eq. (6) is shown in column 3 of Table 1. The calculated  $\text{TIC}^{-1}$  reproduces the farfield measurement of the  $\text{TIC}^{-1}$ , using the averaged intensity, very well. A slight difference for the multipass amplifiers is due to the characterization of the amplifiers as one unit. Here, Pockels cells between the amplifiers increase the  $\text{TIC}^{-1}$  of the multipass amplifiers by reducing the total ASE energy, which was measured behind the compressor. From this consideration it follows, that the presented model is not only suitable for estimating the  $\text{TIC}^{-1}$  of a RA, but also for estimating the  $\text{TIC}^{-1}$  of multipass amplifiers within the far-field of the main pulse.

### Various solid state laser materials

For a comprehensive understanding of the ASE generation, the influence of different solid state materials has to be studied. Since Eq. (9), valid for the introduced minimum small signal gain,  $\bar{g} = \bar{g}_{\text{min}}$ , shows a dependence on material and main pulse parameters only, a comparative study of different types of solid state amplifier materials is possible. Here, solid state materials supporting  $\tau_{\text{pulse}} \leq 350$  fs, were analyzed using Eq. (9) with  $E_{\text{seed}} = 1$  nJ. To ensure the comparability of the  $\text{TIC}^{-1}$  for different pulse durations, the spectral acceptance range was defined by the doubled bandwidth calculated by the time bandwidth product for a Gaussian shaped pulse:

$$\Delta\nu = 2 \times \frac{2 \ln 2}{\pi} \frac{1}{\tau_{\text{pulse}}} \quad (13)$$

For the study,  $\bar{I}_{\text{sat}}$ ,  $K_{\Delta\nu}$  and  $K_p$  were calculated using spectroscopic data from the literature. The used parameters

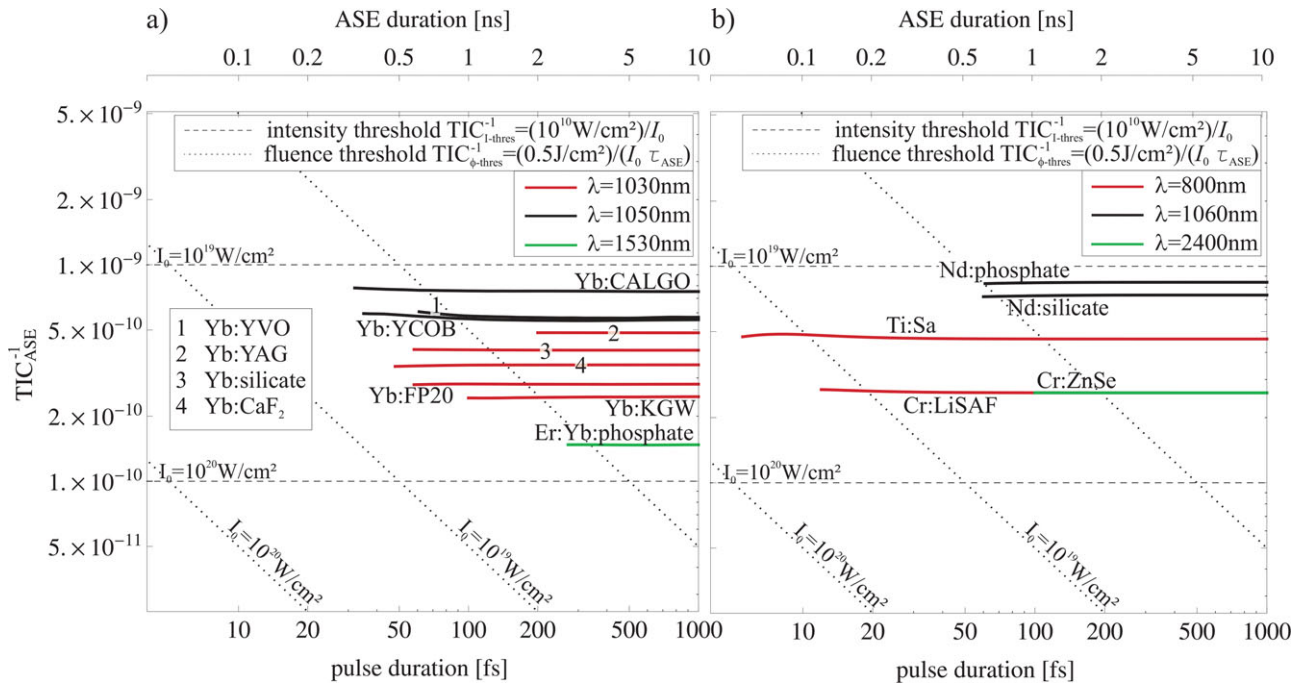


**Figure 4** Comparative study of the  $TIC^{-1}$  for various low-gain Yb-doped materials (a) [35–49] and state-of-the-art high-gain laser materials (b) [50–57] indicated by the solid lines over the pulse duration up to a minimum duration realized in a mode-locked operation; intensity threshold of  $I_{thres} = 10^{10} \text{ W/cm}^2$  (horizontal dashed lines) and fluence threshold of  $F_{thres} = 0.5 \text{ J/cm}^2$  (diagonal, dashed lines) for focussed intensity of  $I_0 = 10^{19} \text{ W/cm}^2$  and  $I_0 = 10^{20} \text{ W/cm}^2$ . The ASE duration  $\tau_{ASE}$  is indicated on the upper horizontal axis. Different colors indicate different laser wavelengths at which the materials can be operated.

are presented in Table 2 for the maximum pulse duration of  $\tau_{pulse} = 350 \text{ fs}$ .

In Fig. 4, we plot the calculated  $TIC^{-1}$  values for different solid state laser materials as a function of the pulse duration up to a minimum duration realized in a mode-locked operation. Note that the  $TIC^{-1}$  obtained for pulses of minimum duration can deteriorate significantly when strong spectral losses need to be introduced during the amplification process to achieve a sufficiently broad bandwidth after full amplification. It is shown that the minimal achievable  $TIC^{-1}$  is independent of the pulse duration since the spectral acceptance of the RA is carefully adapted to the designed pulse duration. Weak  $TIC^{-1}$  modulations in the range of the minimum pulse duration can occur due to significant modulations of the spectroscopic properties of the material.

Since the ratio of the Einstein coefficients [34] for spontaneous emission  $A_{21}$  and stimulated emission  $B_{21}$

$$\frac{A_{21}}{B_{21}} = \frac{8\pi h}{\lambda^3} \quad (14)$$

shows a  $\lambda^{-3}$  dependency and the spatial acceptance of the amplifier is proportional to  $\lambda^2$ , a  $1/\lambda$ -dependence of the  $TIC^{-1}$  was expected. Ivanov et al. have proven this correlation by deriving the Schawlow-Towns criterion from Eq. (4) by replacing the emission cross section with the Füchtbauer-Ladenburg equation [27]. However, a clear

**Table 2** Spectroscopic parameters for the different solid state laser materials considered in Fig. 4. All parameters are given for a spectral bandwidth sufficient for the minimum considered pulse duration of  $\tau = 350 \text{ fs}$  according to Eq. (13).

Material	$\lambda$ [ $\mu\text{m}$ ]	$\bar{I}_{sat}$ [ $\frac{\text{kW}}{\text{cm}^2}$ ]	$K_p$	$K_{\Delta\nu}$	Refs
<i>Rare-earth doped materials</i>					
Yb:FP20	1.03	38.0	0.5	0.05	[10, 45]
Yb:CaF <sub>2</sub>	1.03	32.5	0.5	0.07	[41, 43]
Yb:YAG	1.03	12.2	0.5	0.27	[41, 42]
Yb:KGW (E  a)	1.03	24.4	0.8	0.04	[46, 47]
Yb:silicate	1.03	38.8	0.5	0.07	[44, 45]
Yb:YVO (E  c)	1.05	176	0.5	0.02	[37, 38]
Yb:YCOB (E  c)	1.05	47.4	0.8	0.05	[39, 40]
Yb:CALGO (E   $\sigma$ )	1.05	65.4	0.7	0.06	[35, 36]
Er:Yb:glass	1.53	1.12	0.5	0.40	[48, 49]
Nd:phosphate	1.06	15.9	0.5	0.30	[50, 51]
Nd:silicate	1.06	20.2	0.5	0.27	[50, 51]
<i>Transition-metal doped materials</i>					
Ti:Sa (E   $\pi$ )	0.80	151	0.7	0.02	[52, 53]
Cr:LiSAF (E   $\pi$ )	0.80	77.8	0.7	0.03	[54, 55]
Cr:ZnSe	2.40	16.4	0.5	0.04	[56, 57]

dependence of the  $\text{TIC}^{-1}$  on the laser wavelength, indicated by the colors in Fig. 4, could not be found. For example the  $\text{TIC}^{-1}$  difference of Cr:LiSAF to Cr:ZnSe (c.f. Fig. 4b) is negligible while the laser wavelengths differ by a factor of 3. Hence, the individual spectroscopic material properties have the strongest influence on the  $\text{TIC}^{-1}$  for the different materials.

In Fig. 4a) various types of  $\text{Yb}^{3+}$ -doped materials, suitable for direct diode pumping are plotted. Here, only a slight difference of up to a factor of 3 has been found for the  $\text{TIC}^{-1}$  level of materials with a central wavelength of  $\lambda \approx 1030 \text{ nm} \dots 1050 \text{ nm}$ . Materials with a low saturation intensity, e.g. Yb:YAG, provide a narrow spectral emission bandwidth which leads to a higher value of  $K_{\Delta\nu}$ . Er:Yb:phosphate with a central wavelength of  $\lambda = 1530 \text{ nm}$  reaches the lowest level due to its long radiation lifetime of  $\tau_{\text{rad}} = 9.5 \text{ ms}$ . Here, however, the bandwidth is limited to a value sufficient for a minimal pulse duration of  $\tau_{\text{pulse}} = 261 \text{ fs}$  only [49].

High-gain materials such as Ti:Sapphire and Nd:glass are plotted in Fig. 4b). Compared to the  $\text{Yb}^{3+}$ -doped materials, the emission cross sections are higher by about one order of magnitude for Nd:glass and two orders of magnitude for Ti:Sapphire. However, the radiation life times range only from  $4 \mu\text{s}$  for Ti:Sapphire to  $370 \mu\text{s}$  for Nd:phosphate glass leading to a higher saturation intensity. Therefore, the resulting  $\text{TIC}^{-1}$  is worse by a factor of 1.6 for Ti:Sapphire and 3.1 for Nd:phosphate glass as compared to Yb:FP20 with  $\tau_{\text{rad}} = 1.4 \text{ ms}$ . From this study, it is shown that the laser material has only a slight influence on the  $\text{TIC}^{-1}$  of a certain laser amplifier.

### 3. The amplification of ASE

As it was shown in the previous section, each individual amplifier of a laser system contributes individually to the total ASE. However, the contribution from the power amplifiers is often much lower than that from the front-end amplifiers, which increase the laser pulse energy to the  $\mu\text{J}$  or  $\text{mJ}$ -level. Hence, for the description of the total ASE, a description of the temporal gain characteristic of the ASE from the first amplifier (or in most cases, the first two amplifiers) is sufficient. Here, the fluence of the generated ASE ( $F = E/A$ ) is orders of magnitude lower than the fluence of the main pulse. As a consequence, the ASE does not reduce the inversion significantly and the temporal characteristic of the ASE is determined by the time dependent gain of the main pulse. Assuming a Gaussian-shaped main pulse, valid both for the compressed and the stretched main pulse, it is evident, that the rising edge of the main pulse experiences a higher gain than the main part of the main pulse due to its lower fluence. Hence, the part of the ASE which comes before the main pulse at  $t < t_0$ , with  $t_0$  corresponding to the peak intensity of the main pulse, is amplified more than the main pulse itself eventually leading to a  $\text{TIC}^{-1}$  deterioration (TD). For the sake of simplicity, losses will be neglected during the following estimation.

To quantify the time-dependent  $\text{TIC}^{-1}$  deterioration  $\text{TD}(t)$ , the time-dependent gain  $g(t)$  has to be compared to the total gain  $g_{\text{total}}$  of the main pulse, i.e.  $\text{TD}(t) = g(t)/g_{\text{total}}$ , for each pass of the amplification. This can be done by considering the non-linear photon transport equations for laser amplification, which were derived by Lee M. Frantz and John S. Nodvik (Eqs. (27) and (28) in [58]). Assuming a Gaussian-shaped main pulse with duration  $\tau$ , described by the photon density  $\Phi_{\text{in}}(x, t) = \Phi_0 \exp(-t^2/\tau^2)$ , and a homogeneous initial inversion  $N_0(x, t) = N_0$  (c.f. eq (2)), the time-dependent main pulse gain  $g(t) = \Phi_{\text{out}}(t)/\Phi_{\text{in}}(t)$  can be expressed by

$$g(t) = \left\{ 1 - \exp \left( -\frac{1}{2} \frac{F_{\text{in}}}{F_{\text{sat}}} \left( 1 + \operatorname{erf} \left[ \frac{t}{\tau} \right] \right) \right) \left( 1 - \frac{1}{g_0} \right) \right\}^{-1}. \quad (15)$$

Here,  $F_{\text{in}}$  is the seed fluence defined by  $F_{\text{in}} = h\nu \sqrt{\pi} c\tau \Phi_0$ , and  $F_{\text{sat}}$  is the saturation fluence of the laser material.  $c$  is the speed of light. The total gain  $g_{\text{total}} = \int_{-\infty}^{\infty} \Phi_{\text{out}}(x, t) dt / \int_{-\infty}^{\infty} \Phi_{\text{in}}(x, t) dt$  of the main pulse can be calculated to

$$g_{\text{total}} = 1 + \frac{F_{\text{sat}}}{F_{\text{in}}} \ln \left( g_0 - (g_0 - 1) \exp \left( -\frac{F_{\text{in}}}{F_{\text{sat}}} \right) \right). \quad (16)$$

With each amplification pass  $n$ , the main pulse is amplified by the gain factor,  $g_{\text{total}}^{(n)}$ , of the  $n^{\text{th}}$  pass and the inversion is reduced according to the respective extraction efficiency,  $\eta_{\text{ex}}^{(n)} = (N_{n+1} - N_n)/N_0$ , which depends on the input fluence of the  $n^{\text{th}}$  pass. Hence, for the total  $\text{TIC}^{-1}$  deterioration of an amplifier, the deterioration of each pass has to be taken into account. However, considering only the relevant part of the ASE at times  $t < t_0$  we found that it is sufficient to consider the energy extraction of one single pass with an appropriate total extraction efficiency of the amplifier of  $\eta_{\text{ex}} = \sum_{n=1}^{\text{passes}} \eta_{\text{ex}}^{(n)}$ . For one amplification pass,  $F_{\text{in}}/F_{\text{sat}}$  can be expressed by

$$\frac{F_{\text{in}}}{F_{\text{sat}}} = \ln \left[ 1 + \frac{\eta_{\text{ex}}}{g_0(1 - \eta_{\text{ex}})} \right] \quad (17)$$

leading to

$$\text{TD}(t) = \left\{ g_0 + (1 - g_0) \left( 1 + \frac{\eta_{\text{ex}}}{g_0(1 - \eta_{\text{ex}})} \right)^{-\frac{1}{2}(1 + \operatorname{erf}[\frac{t}{\tau}])} \right\}^{-1} \cdot g_0 \left( 1 - \frac{\ln \left( 1 - \eta_{\text{ex}} + \frac{\eta_{\text{ex}}}{g_0} \right)}{\ln(1 - \eta_{\text{ex}})} \right). \quad (18)$$



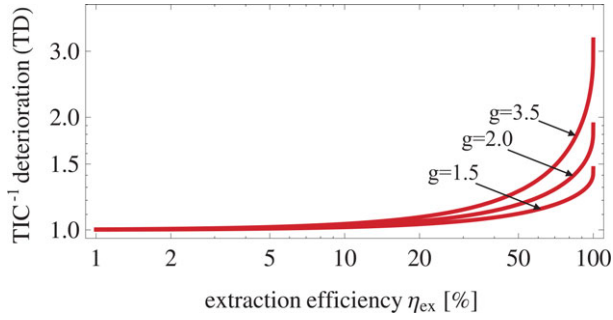


**Figure 5** Double logarithmic scale of the temporal intensity contrast deterioration (TD) during the amplification of the main pulse with respect to the extraction efficiency of the laser amplifier for gain values of  $g_0 = 1.5, 2.0$  and  $3.5$ .

If only the maximal  $\text{TIC}^{-1}$  deterioration is of interest, Eq. (18) simplifies to

$$TD(t \rightarrow -\infty) = g_0 \left( 1 - \frac{\ln \left( 1 - \eta_{\text{ex}} + \frac{\eta_{\text{ex}}}{g_0} \right)}{\ln(1 - \eta_{\text{ex}})} \right). \quad (19)$$

Eq. (19) is plotted in Fig. 5 for gain values of  $g_0 = 1.5, 2.0$  and  $3.5$ . Since for small extraction efficiencies no significant saturation can be observed, the  $\text{TIC}^{-1}$  deterioration is negligibly small. However, for high extraction efficiencies, a  $\text{TIC}^{-1}$  deterioration is obvious. Considering the theoretical limit of  $\eta_{\text{ex}} \rightarrow 1$ , the  $\text{TIC}^{-1}$  deterioration becomes almost as large as the small signal gain  $\text{TD}_{t \rightarrow -\infty} \rightarrow g_0$ . Note that the  $\text{TIC}^{-1}$  calculation according to Eq. (18) leads to a significant overestimation of the  $\text{TIC}^{-1}$  for  $t > t_0$  due to the simplified consideration of one single pass only.

From Eq. (4) it follows that the ASE, which is generated within the stretched or unstretched main pulse at times  $t \sim t_0$ , has a constant level. This was also confirmed by TIC measurements of the compressed main pulse at the unsaturated POLARIS-System, where we measured no difference of the ASE-level before and after the main pulse. However, if saturation occurs, the ASE-level shows a continuous decrease during the main pulse due to saturation effects, which strongly depends on the temporal shape of the stretched or unstretched main pulse (e.g. Gaussian or top-hat). However, since the temporal shape differs from pass to pass and depends strongly on the population inversion and the respective fluence of the seed pulse, an individual characterization of each laser system becomes inevitable.

#### 4. Intensity scaling of a high-contrast front-end

With the presented model, it is possible to design a high-contrast (low inverted contrast) front-end, which meets the intensity and fluence thresholds for a high-intensity laser system interacting with thin foils, mostly metal,

as described by Kalashnikov et al. [59]. In Fig. 4, the intensity threshold of  $I_{\text{thres}} = 10^{10} \text{ W/cm}^2$  for prepulses is given by the horizontal, dashed lines for focussed intensities of  $I_0 = 10^{19} \text{ W/cm}^2$  and  $I_0 = 10^{20} \text{ W/cm}^2$ , respectively. The fluence threshold of  $F_{\text{thres}} = 0.5 \text{ J/cm}^2$  [59] is given by the diagonal, dotted lines for the same peak intensities. The corresponding values for  $\tau_{\text{ASE}}$  are given by the upper axis. It can be seen, that for focussed intensities of  $I_0 \geq 10^{20} \text{ W/cm}^2$  the critical thresholds can only be achieved by significantly increasing the seed energy or additional temporal contrast cleaning techniques such as XPW, OPA or plasma mirrors. Since the output energy of state-of-the-art oscillators is limited by the damage thresholds of the optics and the stability condition of the cavity, contrast cleaning techniques are inevitable for high-intensity laser systems. For this purpose, the presented study represents a helpful tool for the estimation of the necessary additional factor of contrast improvement.

Fig. 6 shows the scaling of this necessary additional contrast improvement of a high-contrast front-end with respect to the focussed main pulse intensity without saturation. On the one hand, the  $\text{TIC}^{-1}$  of the front-end amplifier has to be improved. On the other hand, the “clean” output energy of the high-contrast front-end has to be sufficiently high so that the ASE generated by all subsequent amplifiers does not exceed the fluence threshold. Hence, for the calculation in Fig. 6 an ASE was assumed, which is generated by the front-end and all subsequent amplifiers in equal parts. Again, for this total ASE, a fluence threshold of  $F_{\text{thres}} = 0.5 \text{ J/cm}^2$  was defined. The left axis shows the necessary  $\text{TIC}^{-1}$  improvement depending on the desired focussed intensity of the main pulse. It is normalized

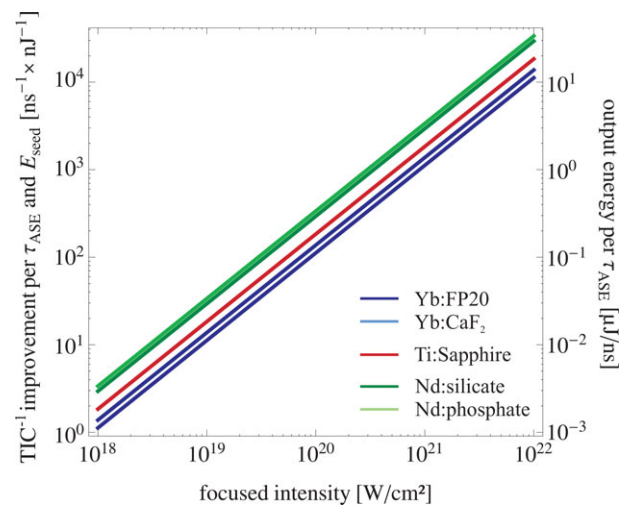


**Figure 6** Scaling of the necessary contrast enhancement of a frontend setup with respect to a desired focussed intensity. The contrast enhancement is shown relative to the ASE duration  $\tau_{\text{ASE}}$  and the oscillator seed energy  $E_{\text{seed}}$ . The right axis presents the desired output energy as the necessary seed energy for the subsequent amplifiers so that the ASE, generated by these amplifiers, does not exceed the fluence threshold. A threshold of  $F_{\text{thres}} = 0.5 \text{ J/cm}^2$  was assumed.

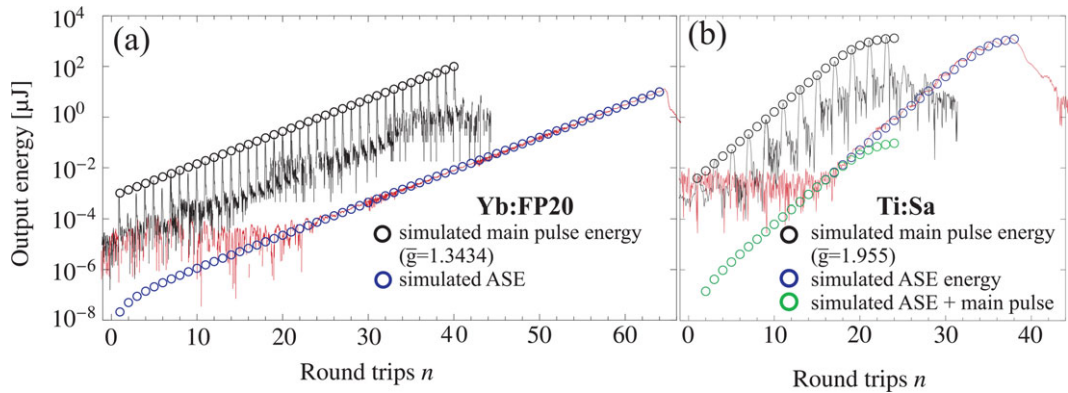


**Figure 7** Amplification characterization of the first regenerative amplifier of the POLARIS (a) and the JETI200 system (b), photo diode measurement of the circulating pulse referenced to the output energy (black line) and the appropriate amplification simulation (black circles); energy calibrated photo diode measurement of the ASE while the seed was blocked at the entrance (red line) and the appropriate ASE simulation according to Eq. (4) with seed pulse (green circles) and with the seed pulse blocked (blue circles).

to  $\tau_{\text{ASE}} = 1$  ns and a “clean” seed energy of  $E_{\text{seed}} = 1$  nJ. This allows for a quick estimation of the necessary  $\text{TIC}^{-1}$  improvement for several seed energies and ASE durations. The right axis shows the “clean” output energy as the necessary seed for the subsequent amplifiers. Note that optical components having only a limited transmission, e.g. grating stretchers with typically  $\eta \approx 10\%$ , have to be considered separately.

For example, a Yb:FP20 laser system, such as POLARIS, designed for a focussed intensity of  $I_0 = 10^{22}$  W/cm<sup>2</sup>, needs a high-contrast front-end including a  $\text{TIC}^{-1}$  enhancement by a factor of  $2.8 \times 10^4$  considering an oscillator energy of  $E_{\text{osc}} = 2$  nJ and an ASE duration of  $\tau_{\text{ASE}} = 5$  ns, as limited by the rise time  $t_{\text{rise}}$  of Pockels cells [60]. Note that the ASE duration cannot be reduced by Pockels cells to less than  $\tau_{\text{stretched}} + t_{\text{rise}}$ , since the pulse is temporally stretched to a duration of  $\tau_{\text{stretched}}$ . If the necessary improvement should be realized with a DCPA including XPW, an efficiency of at least 13% is necessary when state-of-the-art polarizers with an extinction ratio of  $5 \times 10^6$  [61] are utilized. This was recently demonstrated with POLARIS [61]. Furthermore, the high-contrast front-end has to provide a “clean” output energy of  $E_{\text{out}} = 56$  μJ so that the ASE, generated by the subsequent amplifiers in addition to the front-end ASE does not exceed the fluence threshold of  $F_{\text{thres}} = 0.5$  J/cm<sup>2</sup>. However, since the stretcher, positioned directly behind the front-end, has a transmission of only  $\sim 10\%$ , the energy output of the high-contrast front-end needs to be increased to  $E_{\text{out}} = 560$  μJ if the main pulse is to be focussed to an intensity of  $I_0 = 10^{22}$  W/cm<sup>2</sup>.

From Fig. 6, it is also possible to recalculate the effective on-target ASE fluence in an experimental setup with a given focussed intensity.

## 5. Experimental validation

In order to experimentally validate the presented model, the ASE of a common Ti:Sapphire based linear RA, such

as that implemented in the JETI200 system ( $P_0 = 200$  TW), and of a regenerative ring amplifier based on Yb<sup>3+</sup>:FP20-glass, operated in the POLARIS system ( $P_0 = 100$  TW, c.f. Fig. 1 in [13]), were both simulated and measured. JETI200 is a double CPA system with a XPW filter between the CPA stages. CPA 1 is seeded by a pre-amplified oscillator pulse and consists of a grating stretcher, a RA, a multipass amplifier and a grating compressor. Subsequently, the pulse is temporally cleaned by XPW and further amplified within CPA 2. The linear RA within CPA 1 (further referred to as JETI200-RA) operates in saturation and amplifies the temporally stretched pulses from an energy of  $E_{\text{seed}} = 2$  nJ to an output energy of  $E_{\text{out}} = 1.4$  mJ within 24 round trips. The POLARIS-RA amplifies the unstretched oscillator pulse from an energy of  $E_{\text{seed}} = 1$  nJ to an output energy of  $E_{\text{out}} = 100$  μJ within 39 round trips.

To evaluate Eq. (4) for both amplifiers, the parameters  $\bar{I}_{\text{sat}}$ ,  $K_{\Delta v}$  and  $K_p$  have to be determined both for Yb:FP20 and for Ti:Sapphire. Here, the spectral acceptance of the POLARIS-RA, c.f. Fig. 2, is 40 nm (1010 nm . . . 1050 nm) around the center wavelength of  $\lambda = 1030$  nm while the JETI200-RA provides 100 nm (750 nm . . . 850 nm) around  $\lambda = 795$  nm. This results in  $K_{\Delta v} = 0.23$  for Yb:FP20 and  $K_{\Delta v} = 0.425$  for Ti:Sapphire. Note that  $K_{\Delta v}$  is  $\sim 2$  times larger than assumed in Eq. (13) for both amplifiers. The mean saturation intensity, averaged over the spectral bandwidth, for Ti:Sapphire with  $\tau_{\text{rad}} = 4$  μs is  $\bar{I}_{\text{sat, Ti:Sapphire}} = 240$  kW/cm<sup>2</sup> [52] considering  $\pi$ -polarization, the corresponding polarization acceptance factor is  $K_p \text{Ti:Sapphire} = 0.71$ . The saturation intensity of Yb:FP20 is  $\bar{I}_{\text{sat, Yb:FP20}} = 35.8$  kW/cm<sup>2</sup> [10] and the material is isotropic which leads to  $K_p \text{Yb:FP20} = 0.5$ .

Both RAs support the amplification of the fundamental mode only, hence the TEM<sub>00</sub>-mode was assumed. However, due to the linear architecture of the JETI200-RA, fluorescence is accepted in both directions of circulation. In a ring cavity, the fluorescence, which is emitted opposite to the circulation direction of the main pulse, is coupled out in a different direction than the main pulse. Hence,

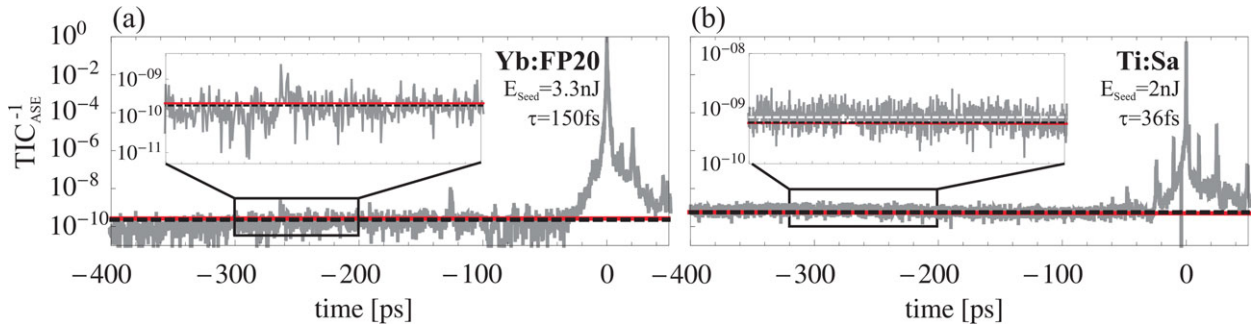


**Figure 8** 3<sup>rd</sup>-order cross-correlation measurement (Sequoia, *Amplitude Technologies*) of the  $\text{TIC}^{-1}$  (gray solid line) of the POLARIS-RA (a) and the JETI200-RA (b) respectively; numerical calculation of the  $\text{TIC}_{\text{ASE}}^{-1}$  using Eq. (4) (red solid line);  $\text{TIC}^{-1}$  estimation by Eq. (6) (black dashed line). The white dashed line in (b) shows the  $\text{TIC}^{-1}$  calculation of the JETI200-RA taking into account the seeded ASE from the preamplifier.

the acceptance solid angle of the JETI200-RA is twice as large as compared to the POLARIS-RA which is built as a ring cavity. The small signal gain was measured to be  $\bar{g}_{0\text{JETI200}} = 1.955$  and  $\bar{g}_{0\text{POLARIS}} = 1.3434$ . Note that since Yb:FP20 operated at room temperature is a quasi-3-level system, reabsorption has to be taken into account. Therefore, a loss term of  $\bar{L} = 1 - \exp[-N_{\text{dop}}\sigma_{\text{abs}}d] + \bar{L}_{\text{cav}}$  was considered for the simulation of the POLARIS-RA, where  $N_{\text{dop}} = 6 \times 10^{20} \text{ cm}^{-3}$ ,  $\sigma_{\text{abs}} = 1.6 \times 10^{-22} \text{ cm}^2$  and  $d = 13 \text{ mm}$ . Furthermore, cavity losses of  $\bar{L}_{\text{cav}} = 5\%$  due to spectral shaping [30] have been taken into account. In contrast, due to the negligible reabsorption of Ti:Sapphire at the laser wavelength, no losses were considered for the simulation of the JETI200-RA. Finally, the fluorescence power, emitted in the first pass according to Eq. (4), was calculated to be  $P_1^{\text{F}} = 1.53 \mu\text{W}$  for the POLARIS-RA and  $P_1^{\text{F}} = 15.6 \mu\text{W}$  for the JETI200-RA.

Since the fluorescence power of the first pass cannot be measured accurately, the amplified fluorescence per pass was numerically simulated without considering the main pulse. Therefore, a constant fluorescence power  $P^{\text{F}}$  emitted during each pass was assumed during the round trip time of the respective amplifier, which was measured to be 13.25 ns for the POLARIS-RA and 9.1 ns for the JETI200-RA. Subsequently, the ASE power per pass was integrated over time. The resulting ASE energy per pass  $E_n^{\text{ASE}}$  is depicted by the blue circles in Fig. 7a) for the POLARIS-RA and in Fig. 7b) for the JETI200-RA. The amplified energy of the main pulse  $E_n^{\text{pulse}}$  was also simulated and is shown by the black circles in Fig. 7. The green circles in Fig. 7b) show the calculated ASE energy per pass when the main pulse is present.

In order to validate the simulation, the ASE energy per pass was measured for both RAs. For this purpose, the fraction of the pulse leaking through a cavity mirror was focussed onto a photo diode to measure both the amplification of the seed pulse as well as the amplification of the ASE while the seed pulse was blocked. To increase the dynamics of the measurement, the number of round trips was increased for the ASE measurement. Afterwards, the diode measurement was calibrated with an energy mea-

surement of the outcoupled pulse and ASE, respectively. In Fig. 7a), the measured and energy calibrated pulse- (black solid line) and ASE-characteristics (red solid line) of the POLARIS-RA are shown, while Fig. 7b) shows these characteristics for the JETI200-RA. The significant noise seen during the first round trips can be attributed to the noise level of the photodiode-oscilloscope setup in the lowest measurement range ( $\sim \text{mV}$ -range). Note that due to the linear architecture of the JETI200-RA, the pulse and the ASE could be detected only after every other pass. Eq. (4) very precisely describes the ASE generation within both RAs.

From the ASE simulation in Fig. 7 it is obvious that the energy contrast of the ASE relative to the main pulse reaches a constant value after 5 passes in both amplifiers. This fact confirms the assumption of the limit of the series expansion for the amplifier dynamics to derive Eq. (6). Fig. 8 shows the  $\text{TIC}_{\text{ASE}}^{-1}$  calculated by Eq. (6) (black dashed line), which very precisely matches the  $\text{TIC}^{-1}$  measurement, carried out with a commercial 3<sup>rd</sup>-order cross correlator Sequoia (*Amplitude Technologies*), of the POLARIS-RA (Fig. 8a) (gray solid line). In contrast the  $\text{TIC}_{\text{ASE}}^{-1}$  calculation of the JETI200-RA shows a slight difference to the  $\text{TIC}^{-1}$  measurement in Fig. 8b). Since the JETI200-RA is seeded by an oscillator pulse which was amplified to the  $\mu\text{J}$ -level by a 14-pass preamplifier, the RA is also seeded by this preamplifier's ASE. Estimating the  $\text{TIC}^{-1}$  of the preamplifier with Eq. (6) yields  $\text{TIC}_{\text{pre}}^{-1} = 1.4 \times 10^{-10}$ , while the preamplifier is seeded by an oscillator pulse energy of  $E_{\text{osc}} = 4 \text{ nJ}$ . The white dashed line in Fig. 8b) represents the addition of the contribution of both amplifiers. Here, the calculation shows also a precise agreement with the measurement. Furthermore the  $\text{TIC}^{-1}$  was not influenced by the saturation of any subsequent amplifiers since the output pulse of the JETI200-RA was compressed and measured directly. Since, the estimated  $\text{TIC}^{-1}$  of the RA of  $\text{TIC}_{\text{RA}}^{-1} = 5.6 \times 10^{-10}$  is worse by a factor of 4 compared to the  $\text{TIC}^{-1}$  of the preamplifier, the overall  $\text{TIC}^{-1}$  of the JETI200 DCPA is dominated by the RA. The red solid line in Fig. 8 represents the calculated amplified ASE power from Fig. 7 of both amplifiers, which was scaled to the ASE intensity assuming a comparable focussing of the ASE and the main pulse.

The  $\text{TIC}^{-1}$  of the POLARIS-RA was measured after the output of the RA was temporally stretched and further amplified by another RA. However, since the POLARIS amplifiers are not running in saturation, the  $\text{TIC}^{-1}$  is not affected by the further amplification. Note that in the  $\text{TIC}^{-1}$  measurement of the POLARIS-RA, the seed energy was increased by a factor of 3.3 since an acousto-optic programmable dispersive filter (Dazzler, *Fastlite*) has been removed, which was operating with an efficiency of 24% directly before the POLARIS-RA. Furthermore the oscillator output energy has decreased by 20% during the operation between both measurements.

An influence of the ASE generated by the oscillator could not be observed in any of these amplifiers. This can be explained by the differences in divergence between the ASE and the main pulse, when a Kerr-lens mode locking oscillator [63] is used. Since the RAs are mode sensitive, the carefully adapted mode of the main pulse is well accepted while the amplification of the oscillator's ASE mode is suppressed.

In order to validate the  $\text{TIC}^{-1}$  deterioration due to saturation, a long-term measurement of the JETI40-laser system was carried out. The JETI40 system is a separate laser system providing a peak power of  $P_0 = 40 \text{ TW}$ . The measurement, shown in Fig. 9, includes a 14-pass preamplifier ( $g_0 = 1.7$ ,  $\eta = 17\%$ ), a RA ( $g_0 = 2$ ,  $\eta = 40\%$ ), a 5-pass amplifier ( $g_0 = 3$ ,  $\eta = 66\%$ ) and a 4-pass amplifier ( $g_0 = 3.2$ ,  $\eta = 77\%$ ) which results in a pulse energy of 420 mJ. The final amplifier, which amplifies the pulses to 1.2 J was not included in this measurement. The seed energy of the preamplifier and the RA, which are generating the main part of the ASE, are 4.6 nJ and 3.3 nJ, respectively. Note that be-

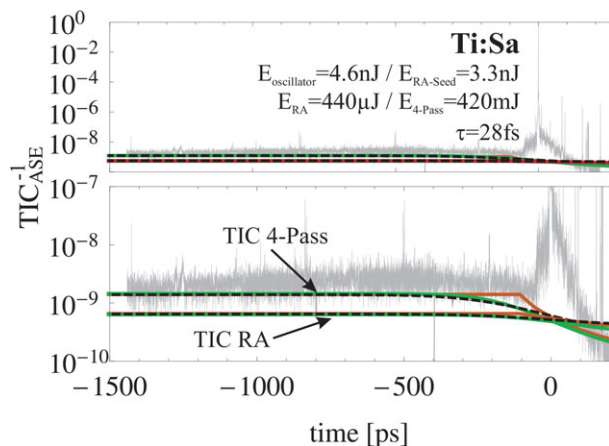


**Figure 9** 3<sup>rd</sup>-order cross-correlation measurement (Sequoia, *Amplitude Technologies*) of the  $\text{TIC}^{-1}$  (gray solid line) of the JETI40 laser system. The measurement shows the  $\text{TIC}^{-1}$  of the amplified pulse including the preamplifier, the RA, a 5-pass and a 4-pass main amplifier. The solid lines represent the numerical simulation of the  $\text{TIC}^{-1}$  of the 5-Pass and the RA assuming a Gaussian (green) and rectangular shaped (red) temporal shape of the main pulse. The black dashed line represents in both cases the  $\text{TIC}^{-1}$  estimation regarding Eq. (6) and (18).

tween both amplifiers, the pulse stretcher and a Dazzler is situated, which limits the energy transmission. The lower black dashed line in Fig. 9 shows the  $\text{TIC}^{-1}$  which was calculated by eqs. (6) and (18) for the main pulse amplified by the preamplifier and the RA, while the upper black dashed line shows the  $\text{TIC}^{-1}$  calculation for all amplifiers included in the measurement. Since the  $\text{TIC}^{-1}$  of the main pulse after the RA was calculated to be  $\text{TIC}_{\text{after-RA}}^{-1} = 5.3 \times 10^{-10}$  at  $t = -1.5 \text{ ns}$ , the  $\text{TIC}^{-1}$  after the 4-pass was calculated to be  $\text{TIC}_{\text{after-4pass}}^{-1} = 1.2 \times 10^{-9}$  which is worse by more than a factor of 2. Note that in comparison to Fig. 8, the  $\text{TIC}_{\text{after-RA}}^{-1}$  at JETI40 is further deteriorated due to cavity losses for spectral shaping of 9.5%. The solid lines in Fig. 9 represent the numerical calculation assuming a Gaussian (green) and a rectangular (red) pulse shape. The different simulations fit well to the measurement for  $t \geq 1 \text{ ns}$  before the arrival of the main pulse. The deviations for  $1 \text{ ns} \geq t \geq t_0$  are likely due to the presence of prepulses, which can clearly be seen in the measurement. The deviations of the simulation within the time range of the main pulse  $t \sim t_0$  can be explained by the actual temporal shape of the main pulse. Here, a rectangular shape leads to a stronger decay of the ASE than for a Gaussian main pulse. Since the temporal shape changes significantly during the amplification, the  $\text{TIC}^{-1}$  estimation by Eq. (18), which assumes a constant temporal Gaussian shape, shows a strong deviation from the measurement.

## 6. Conclusions & Outlook

In conclusion, we have presented an advanced model to calculate the temporal intensity contrast in high-intensity laser systems including the generation and the amplification of the ASE. The model was validated at three different high-power laser systems. Detailed measurements are in excellent agreement with the model. The applicability for different types of amplifiers regarding the contrast in the far-field was demonstrated too and has also been confirmed by measurements. All relevant parameters were discussed and it was found that a minimal gain is necessary to overcome significant deterioration of the temporal intensity contrast due to amplifier losses. In addition, a narrow confinement of the spectral acceptance of an amplifier with respect to the final compressed pulse duration is necessary for a contrast-optimized amplifier design. A comparative study containing various types of solid state laser materials supporting the amplification of pulse durations  $\leq 350 \text{ fs}$  was presented. The different laser materials only show slight differences regarding the optimally achievable contrast. A general correlation to the laser wavelength, as it could intuitively be expected from the Einstein coefficients, could not be found. The temporal intensity contrast estimated within this study was compared to common intensity and fluence threshold values, which allows to determine the requirements of a high-contrast laser front-end regarding the contrast improvement and the necessary “clean” output energy.

With the exciting future prospect of the realization of large-scale, high-power laser systems, peak powers of 10 PW and more and on-target intensities of  $10^{23} \text{ W/cm}^2$

and beyond will come into reach. These systems are currently designed and set up to achieve controllable conditions in a laboratory setting. This enables performing repeatable experimental studies, to discover fundamentally new physical phenomena, and to further push the achievable particle energies far into the ultra-relativistic regime. Since these experiments often require ever increasing intensities and at the same time more sophisticated target designs, the future requirements for the laser contrast will be even stricter. For this purpose, the presented study will be an indispensable tool for the careful design of these future high-power laser systems.

**Acknowledgement.** The authors thanks B. Beleites and F. Ronneberger for patiently measuring the JET140 contrast. Furthermore, we thank F. Karbstein for mathematical support and inspiring conversations and M. Schwab for the quick and thorough review of the manuscript. The research leading to these results has received funding from the European Commission's (EC's) 7th Framework Programme (LASERLAB-EUROPE, grant no. 228334) and from the Bundesministerium für Bildung und Forschung (BMBF) (03ZIK445 and 03Z1H531).

**Received:** 6 August 2015, **Revised:** 2 November 2015,

**Accepted:** 25 November 2015

**Published online:** 30 December 2015

**Key words:** Amplified spontaneous emission, ASE, temporal intensity contrast, high power lasers, laser amplifiers, regenerative amplifier, CPA, modelling, laser plasma interaction.

## References

- [1] E. Esarey, C. B. Schroeder, and W. P. Leemans, *Rev. Mod. Phys.* **81**, 1229 (2009).
- [2] A. Macchi, M. Borghesi, and M. Passoni, *Rev. Mod. Phys.* **85**, 751 (2013).
- [3] T. Popmintchev, M.-C. Chen, P. Arpin, M. M. Murnane, and H. C. Kapteyn, *Nature Photon.* **4**, 822 (2010).
- [4] S. V. Bulanov, T. Zh. Esirkepov, V. S. Khoroshkov, A. V. Kuznetsov, and F. Pegorato, *Phys. Lett. A* **299**, 240 (2002).
- [5] V. Yanovsky, V. Chvykov, G. Kalinchenko, P. Rousseau, T. Planchon, T. Matsuoka, A. Maksimchuk, J. Nees, G. Cheriaux, G. Mourou, and K. Krushelnick, *Opt. Express* **16**, 2110 (2008).
- [6] T. J. Yu, S. K. Lee, J. H. Sung, J. W. Yoon, T. M. Jeong, and J. Lee, *Opt. Express* **20**, 10807 (2012).
- [7] D. Strickland and G. Mourou, *Opt. Commun.* **56**, 219 (1985).
- [8] E. W. Gaul, M. Martinez, J. Blakeney, A. Jochmann, M. Ringuette, D. Hammond, T. Borger, R. Escamilla, S. Douglas, W. Henderson, G. Dyer, A. Erlandson, R. Cross, J. Caird, C. Ebberts, and T. Ditmire, *Appl. Opt.* **49**, 1676 (2010).
- [9] Y. Chu, X. Liang, L. Yu, Y. Xu, L. Xu, L. Ma, X. Lu, Y. Liu, Y. Leng, R. Li, and Z. Xu, *Opt. Express* **21**, 29231 (2013).
- [10] D. Eht and T. Töpfer, *Proceedings of SPIE* **4102**, 95 (2000).
- [11] M. Siebold, S. Bock, U. Schramm, B. Xu, J. L. Doualan, P. Camy, and R. Moncorgé, *Appl. Phys. B* **97**, 327 (2009).
- [12] A. Kessler, M. Hornung, S. Keppler, F. Schorcht, M. Hellwing, H. Liebetrau, J. Körner, A. Sävert, M. Siebold, M. Schnepf, J. Hein, and M. C. Kaluza, *Opt. Lett.* **39**, 1333 (2014).
- [13] M. Hornung, H. Liebetrau, A. Seidel, S. Keppler, A. Kessler, J. Körner, M. Hellwing, F. Schorcht, D. Klöpfel, A. K. Arunachalam, G. A. Becker, A. Sävert, J. Polz, J. Hein, and M. C. Kaluza, *High Power Laser Sci. Eng.* **2**, e20 (2014).
- [14] M. C. Kaluza, J. Schreiber, M. I. K. Santala, G. D. Tsakiris, K. Eidmann, J. Meyer-ter-Vehn, and K. J. Witte, *Phys. Rev. Lett.* **93**, 045003 (2004).
- [15] M. P. Kalashnikov, E. Risse, H. Schönnagel, and W. Sandner, *Opt. Lett.* **30**, 923 (2005).
- [16] A. Jullien, O. Albert, F. Burgy, G. Hamoniaux, J.-P. Rousseau, J.-P. Chambaret, F. Augé-Rochereau, G. Chériaux, J. Etchepare, N. Minkovski, and S. M. Saltiel, *Opt. Lett.* **30**, 920 (2005).
- [17] J. Itatani, J. Faure, M. Nantel, G. Mourou, and S. Watanabe, *Opt. Commun.* **148**, 70 (1998).
- [18] H. Yoshida, E. Ishii, R. Kodama, H. Fujita, Y. Kitagawa, Y. Izawa, and T. Yamanaka, *Opt. Lett.* **28**, 257 (2003).
- [19] H. C. Kapteyn, M. M. Murnane, A. Szoke, and R. W. Falcone, *Opt. Lett.* **16**, 490 (1991).
- [20] J. M. Mikhailova, A. Buck, A. Borot, K. Schmid, C. Sears, G. D. Tsakiris, F. Krausz, and L. Veisz, *Opt. Lett.* **36**, 3145 (2011).
- [21] S. Keppler, R. Bödefeld, M. Hornung, A. Sävert, J. Hein, and M. C. Kaluza, *Appl. Phys. B* **104**, 11 (2011).
- [22] N. V. Didenko, A. V. Konyashchenko, A. P. Lutsenko, and S. Yu. Tenyakov, *Opt. Express* **16**, 3178 (2008).
- [23] S. Keppler, M. Hornung, R. Bödefeld, M. Kahle, J. Hein, and M. C. Kaluza, *Opt. Express* **20**, 20742 (2012).
- [24] C. Dorrer and J. Bromage, *Opt. Express* **16**, 3058 (2008).
- [25] C. Hooker, Y. Tang, O. Chekhlov, J. Collier, E. Divall, K. Ertel, S. Hawkes, B. Parry, and P. P. Rajeev, *Opt. Express* **19**, 2193 (2011).
- [26] M. Trentelman, I. N. Ross, and N. Danson, *Appl. Opt.* **36**, 8567 (1997).
- [27] V. V. Ivanov, A. Maksimchuk, and G. Mourou, *Appl. Opt.* **42**, 7231 (2003).
- [28] W. Koechner, *Solid-State Laser Engineering* (Springer Science + Business Media, Inc., 2006).
- [29] I. N. Ross, P. Matousek, M. Towrie, A. J. Langley, and J. L. Collier, *Opt. Commun.* **144**, 125 (1997).
- [30] M. Hornung, S. Keppler, R. Bödefeld, A. Kessler, H. Liebetrau, J. Körner, M. Hellwing, F. Schorcht, O. Jäckel, A. Sävert, J. Polz, A. K. Arunachalam, J. Hein, and M. C. Kaluza, *Opt. Lett.* **38**, 718 (2013).
- [31] R. M. Corless, G. H. Gonnet, D. E. G. Hare, D. J. Jeffrey, and D. E. Knuth, *Adv. Comput. Math.* **5**, 329 (1996).
- [32] A. Yariv, *Quantum Electronics* (Wiley, New York, 1988).
- [33] S. Keppler, M. Hornung, R. Bödefeld, A. Sävert, H. Liebetrau, J. Hein, and M. C. Kaluza, *Opt. Express* **22**, 11228 (2014).
- [34] F. Träger, *Handbook of Lasers and Optics* (Springer Science + Business Media, Inc., 2007).
- [35] J. Petit, P. Goldner, and B. Viana, *Opt. Lett.* **30**, 1345 (2005).
- [36] P. Sévillano, P. Georges, F. Druon, D. Descamps, and E. Cormier, *Opt. Lett.* **39**, 6001 (2014).

- [37] Y. K. Voron'ko, V. V. Kochurikhin, A. A. Sobol', S. N. Ushakov, and V. E. Shukshin, *Inorg. Mater.* **40**, 1083 (2004).
- [38] A. A. Lagatsky, A. R. Sarmani, C. T. A. Brown, W. Sibbett, V. E. Kisel, A. G. Selivanov, I. A. Denisov, A. E. Troshin, K. V. Yumashev, N. V. Kuleshov, V. N. Matrosov, T. A. Matrosova, and M. I. Kupchenko, *Opt. Lett.* **30**, 3234 (2005).
- [39] A. Aron, G. Aka, B. Viana, A. Kahn-Harari, D. Vivien, F. Druon, F. Balembois, P. Georges, A. Brun, N. Lenain, and M. Jacquet, *Opt. Mater.* **16**, 181 (2001).
- [40] A. Yoshida, A. Schmidt, V. Petrov, C. Fiebig, G. Erbert, J. Liu, H. Zhang, J. Wang, and U. Griebner, *Opt. Lett.* **36**, 4425 (2011).
- [41] J. Körner, C. Vorholt, H. Liebetrau, M. Kahle, D. Klöpfel, R. Seifert, J. Hein, and M. C. Kaluza, *J. Opt. Soc. Am. B* **29**, 2493 (2012).
- [42] O. Pronin, J. Brons, C. Grasse, V. Pervak, G. Boehm, M.-C. Amann, V. L. Kalashnikov, A. Apolonski, and F. Krausz, *Opt. Lett.* **36**, 4746 (2011).
- [43] G. Machinet, P. Sévillano, F. Guichard, R. Dubrasquet, P. Camy, J.-L. Doualan, R. Moncorgé, P. Georges, F. Druon, D. Descamps, and E. Cormier, *Opt. Lett.* **38**, 4008 (2013).
- [44] K. Lu and N. K. Dutta, *J. Appl. Phys.* **91**, 576 (2002).
- [45] C. Hönninger, F. Morier-Genoud, M. Moser, U. Keller, L. R. Brovelli, and C. Harder, *Opt. Lett.* **23**, 1998 (1998).
- [46] N. V. Kuleshov, A. A. Lagatsky, A. V. Podlipensky, V. P. Mikhailov, and G. Huber, *Opt. Lett.* **22**, 1317 (1997).
- [47] G. Paunescu, J. Hein, and R. Sauerbrey, *Appl. Phys. B* **79**, 555 (2004).
- [48] J. F. Philipps, T. Töpfer, H. Ebendorff-Heidepriem, D. Ehrhart, and R. Sauerbrey, *Appl. Phys. B* **72**, 399 (2001).
- [49] K. H. Fong, K. Kikuchi, C. S. Goh, S. Y. Set, R. Grange, M. Haiml, A. Schlatter, and U. Keller, *Opt. Lett.* **32**, 38 (2007).
- [50] G. R. Hays, E. W. Gaul, M. D. Martinez, and T. Ditmire, *Appl. Opt.* **46**, 4813 (2007).
- [51] J. Aus der Au, D. Kopf, F. Morier-Genoud, M. Moser, and U. Keller, *Opt. Lett.* **22**, 307 (1997).
- [52] P. F. Moulton, *J. Opt. Soc. Am. B* **3**, 125 (1986).
- [53] U. Morgner, F. X. Krtner, S. H. Cho, Y. Chen, H. A. Haus, J. G. Fujimoto, E. P. Ippen, V. Scheuer, G. Angelow, and T. Tschudi, *Opt. Lett.* **24**, 411 (1999).
- [54] S. A. Payne, L. K. Smith, R. J. Beach, B. H. T. Chai, J. H. Tassano, L. D. DeLoach, W. L. Kway, R. W. Solarz, and W. F. Krupke, *Appl. Opt.* **33**, 5526 (1994).
- [55] S. Uemura and K. Torizuka, *Opt. Lett.* **24**, 780 (1999).
- [56] L. D. DeLoach, R. H. Page, G. D. Wilke, S. A. Payne, and W. F. Krupke, *IEEE J. Quantum Electron.* **32**, 885 (1996).
- [57] M. N. Cizmeciyan, J. W. Kim, S. Bae, B. H. Hong, F. Rotermund, and A. Sennaroglu, *Opt. Lett.* **38**, 341 (2013).
- [58] L. M. Frantz and J. S. Nodvik, *J. Appl. Phys.* **34**, 2346 (1963).
- [59] M. Kalashnikov, A. Andreev, and H. Schönagel, *Proceedings of SPIE* **7501**, 750104 (2009).
- [60] S. Keppler, R. Bödefeld, M. Hornung, A. Sävert, J. Hein, and M. C. Kaluza, *Proceedings of SPIE* **8080**, 80800F (2011).
- [61] H. Liebetrau, M. Hornung, A. Seidel, M. Hellwing, A. Kessler, S. Keppler, F. Schorcht, J. Hein, and M. C. Kaluza, *Opt. Express* **22**, 24776 (2014).
- [62] A. Jullien, J.-P. Rousseau, B. Mercier, L. Antonucci, O. Albert, G. Chériaux, S. Kourtev, N. Minkovski, and S. M. Saitiel, *Opt. Lett.* **33**, 2353 (2008).
- [63] T. Brabec, C. Spielmann, P. F. Curley, and F. Krausz, *Opt. Lett.* **17**, 1292 (1992).